

Katanin spiral and ring structures shed light on power stroke for microtubule severing

Elena Zehr¹, Agnieszka Szyk¹, Grzegorz Piszczek², Ewa Szczesna¹, Xiaobing Zuo³ & Antonina Roll-Mecak^{1,4} 

Microtubule-severing enzymes katanin, spastin and fidgetin are AAA ATPases important for the biogenesis and maintenance of complex microtubule arrays in axons, spindles and cilia. Because of a lack of known 3D structures for these enzymes, their mechanism of action has remained poorly understood. Here we report the X-ray crystal structure of the monomeric AAA katanin module from *Caenorhabditis elegans* and cryo-EM reconstructions of the hexamer in two conformations. The structures reveal an unexpected asymmetric arrangement of the AAA domains mediated by structural elements unique to microtubule-severing enzymes and critical for their function. The reconstructions show that katanin cycles between open spiral and closed ring conformations, depending on the ATP occupancy of a gating protomer that tenses or relaxes interprotomer interfaces. Cycling of the hexamer between these conformations would provide the power stroke for microtubule severing.

Cells constantly assemble and disassemble their microtubule cytoskeleton through the concerted action of microtubule polymerases, depolymerases, crosslinkers and severing enzymes. The microtubule-severing enzymes spastin, katanin and fidgetin generate internal breaks in microtubules, thus modulating their dynamics and organization¹. The mechanism used by these enzymes to destabilize the microtubule, a polymer with a flexural rigidity comparable to that of Plexiglas², is still poorly understood. Microtubule-severing enzymes are critical in a wide range of cell biological processes including biogenesis of neuronal and noncentrosomal microtubule arrays^{3–7}, phototropism^{5,7}, spindle scaling^{7–11}, chromosome segregation^{10,12} and control of centriole and cilia numbers^{13–15}. These enzymes are found throughout the animal kingdom, plants and protozoa, and mutations affecting them cause severe neurodegenerative and neurodevelopmental disorders^{1,14–16}. All known microtubule-severing enzymes belong to the family of ATPases associated with various cellular activities called AAA ATPases.

Katanin was the first microtubule-severing enzyme discovered^{17,18}. Fittingly, it was named after the Japanese word *katana*, a celebrated type of samurai sword. Katanin is composed of a catalytic (p60) and a regulatory (p80) subunit. The catalytic subunit contains the AAA ATPase motor and is sufficient for microtubule severing^{10,19}. The p80 subunit regulates association with the centrosome and enhances microtubule binding^{18–21}. ATP hydrolysis is required for severing activity, and katanin p60 ATPase is stimulated by the microtubule¹⁹. The p60 AAA ATPase domain is connected to an N-terminal microtubule interacting and trafficking (MIT) domain through a poorly conserved linker, a sequence arrangement shared with the microtubule-severing enzymes spastin and fidgetin¹. Largely owing to a lack of 3D structures, the mechanism of microtubule severing by this class of enzymes has

remained poorly understood 25 years after the discovery of the first microtubule-severing enzyme^{17,18}. Here we report the first X-ray structure of the monomeric AAA katanin module and cryo-EM reconstructions of the hexamer in two conformations. These structures reveal an unexpected asymmetric arrangement of the AAA domains mediated by structural elements unique to microtubule-severing enzymes and that we show are critical for their function. Cryo-EM reconstructions at 4.4-Å and 6-Å resolution of the katanin hexamer reveal both an open spiral and a closed ring conformation of the AAA core, depending on the nucleotide occupancy of a gating protomer that closes an ~40-Å-wide gate in the katanin hexamer. Together with solution small-angle X-ray scattering (SAXS) reconstructions, our integrated structural study supports a model whereby katanin makes multivalent interactions with the microtubule through its AAA core, flexible MIT domains and a newly defined linker element that crowns the AAA ring and engages the C-terminal tails of tubulin through conserved pore loops that gradually pull tubulin dimers out of the microtubule lattice by cycling between open spiral and closed AAA-ring conformations. Given the high sequence homology, a similar mechanism is probably shared by all microtubule-severing enzymes. Lastly, our integrated study also provides insight into the many katanin mutants identified from classic genetic studies on meiosis in which the katanin gene (also known as *mei-1*) was first identified, as well as hereditary spastic paraplegia mutations found in the microtubule-severing enzyme spastin.

RESULTS

Solution structure of the katanin hexamer

The two microtubule-severing enzymes katanin and spastin assemble into a hexamer in their active ATP-bound states^{1,22}. This hexamer is

¹Cell Biology and Biophysics Unit, Porter Neuroscience Research Center, National Institute of Neurological Disorders and Stroke, Bethesda, Maryland, USA.

²Biophysics Core, National Heart, Lung and Blood Institute, Bethesda, Maryland, USA. ³X-ray Science Division, Advanced Photon Source, Argonne National Laboratory, Argonne, Illinois, USA. ⁴Biochemistry and Biophysics Center, National Heart, Lung and Blood Institute, Bethesda, Maryland, USA. Correspondence should be addressed to A.R.-M. (Antonina@mail.nih.gov).

Received 20 April; accepted 7 July; published online 7 August 2017; doi:10.1038/nsmb.3448

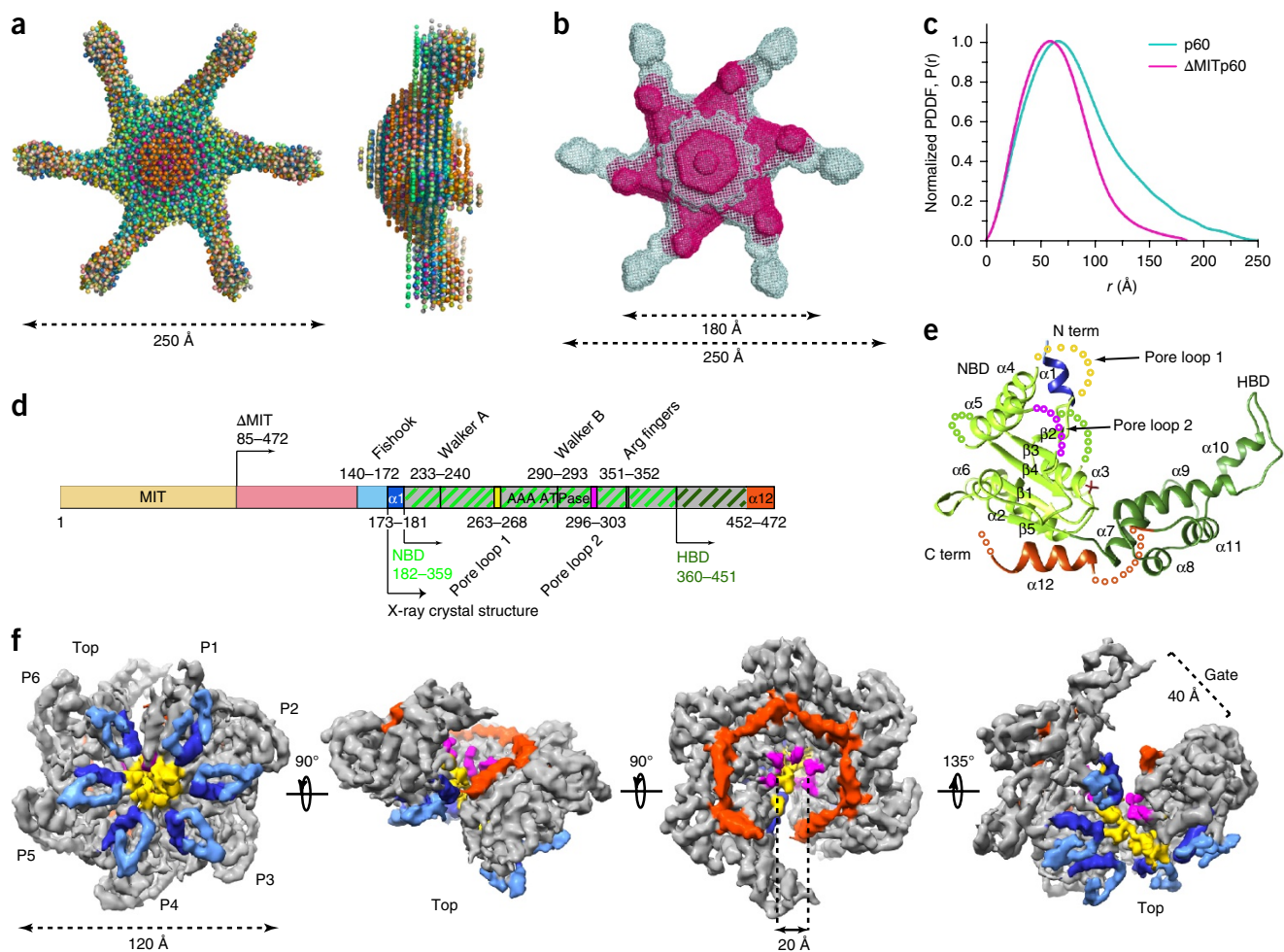


Figure 1 Architecture of monomeric and assembled katanin from X-ray diffraction, solution SAXS and cryo-EM structures. (a) Top and side views of 20 superimposed *ab initio* bead models of full-length katanin p60 calculated from solution SAXS data (Supplementary Fig. 1 and Online Methods). (b) Top view of an overlay of representative models for full-length (gray) and Δ MIT katanin (magenta). Approximate dimensions are shown. (c) Pair-distance distribution functions for full-length and Δ MIT katanin p60. (d) Domain diagram of katanin p60; MIT, microtubule interacting and trafficking domain, yellow; flexible linker, pink; AAA domain, gray; fishhook-shaped linker element, light blue; $\alpha 1$, dark blue; $\alpha 12$ and C-terminal residues 468–472, dark orange. NBD and HBD are highlighted by light green and dark green hatches, respectively. Residue numbers for *C. elegans* katanin. (e) Cartoon representation of the katanin AAA core crystal structure; N-terminal helix $\alpha 1$, blue; NBD, light green; HBD, dark green; C-terminal helix $\alpha 12$, dark orange; sulfate ion as stick representation; unresolved residues shown as spheres. (f) Views of the final sharpened 3D density map (13 σ) of the katanin hexamer filtered to 4.4-Å resolution showing a spiral architecture (rotation angles between the different views indicated with arrows). Top, microtubule-binding face²³. Approximate dimensions are shown. Structural elements color coded as in d. Bracket indicates open gate between P1 and P6.

labile and falls apart at lower protein concentrations²². Consequently, the high-resolution architecture of an assembled microtubule-severing enzyme has remained elusive. Analytical ultracentrifugation (AUC) showed that the catalytic subunit of *C. elegans* katanin (MEI1) populates a mixture of oligomerization states as a function of protein concentration and bound nucleotide. At the highest concentration measured (24 μ M) and in the presence of ATP, the dominant species was a hexamer that dissociated at lower concentrations (Supplementary Fig. 1a,b). Introduction of a commonly used mutation in the Walker B element that retains ATP binding but prevents hydrolysis stabilized the hexamer²² to concentrations as low as 3 μ M (Supplementary Fig. 1c). Solution SAXS measurements of this species (hereafter referred to as katanin) revealed an elongated molecule with a maximal diameter (D_{\max}) of \sim 250 Å (Fig. 1a–c). SAXS *ab initio* reconstructions generated by imposing six-fold symmetry revealed a disc structure \sim 130 Å in diameter with slender arms that fan out at variable angles (Fig. 1a, Supplementary Fig. 1d,e,f,h

and Online Methods), thus indicating a high degree of flexibility. This architecture is reminiscent of the one reported previously for spastin²³. The dimensions of the central ring are compatible with a hexameric assembly of AAA ATPase domains^{23,24}. The MIT domains reside, on average, at the tips of the extended arms, as a deletion construct that lacks this domain (hereafter referred to as Δ MIT katanin, Fig. 1d) had a D_{\max} of \sim 180 Å and shorter arms (Fig. 1b,c and Supplementary Fig. 1g,h).

Asymmetric architecture of the katanin hexamer

To obtain a higher-resolution view of katanin, we employed a hybrid structural approach combining X-ray crystallography of the monomer and cryo-EM of the hexamer. We solved the X-ray structure of the nucleotide-free monomer by X-ray crystallography at 3.3-Å resolution (Fig. 1e and Table 1). This structure showed well-resolved density for only the AAA domain (residues 173–467). It is comprised of an enzymatic α/β nucleotide-binding domain (NBD) that

Table 1 Data collection and refinement statistics

Katanin AAA apo (PDB 5WC1)	
Data collection	
Space group	$P6_5$
Cell dimensions	
a, b, c (Å)	99.4, 99.4, 76.6
α, β, γ (°)	90, 90, 120
Resolution (Å)	50.0–3.2 (3.26–3.20)
R_{sym} (%)	9.8 (56.7)
$I/\sigma(I)$	36.7 (3.4)
Completeness (%)	98.7 (100.00)
Redundancy	9.8 (10.2)
Refinement	
Resolution (Å)	46.0–3.3
No. reflections	7,090
$R_{\text{work}} / R_{\text{free}}$	30.8 / 24.8
No. atoms	
Protein	1,793
Ion (SO ₄)	10
Water	0
B factors	
Protein	107.6
Ligand/ion	177.2
Water	
R.m.s. deviations	
Bond lengths (Å)	0.003
Bond angles (°)	0.573

Data collected from one crystal. Values in parentheses are for highest-resolution shell.

contains the Walker A and B motifs involved in coordinating and hydrolyzing ATP and a helix bundle domain (HBD). The katanin AAA domain differs from that of other AAA ATPases like ClpX, N-ethylmaleimide-sensitive factor (NSF) and heat-shock protein (Hsp) 104 by two helices (N-terminal $\alpha 1$ and C-terminal $\alpha 12$) that augment the NBD and are characteristic of severing enzymes²³ (**Fig. 1d** and **Supplementary Fig. 2**).

We also obtained structures of the assembled full-length katanin hexamer by single-particle cryo-EM (**Table 2**, **Fig. 1f**, **Supplementary Fig. 3** and Online Methods). The data were refined and classified without imposing symmetry, yielding two reconstructions of distinct conformational states at 4.4-Å and 6.0-Å resolution (FSC = 0.143 criterion) (**Supplementary Figs. 3** and **4** and Online Methods). Well-resolved secondary structure elements in both reconstructions allowed determination of pseudoatomic models by flexibly fitting the X-ray structure of the AAA monomer and then applying real-space refinement (**Table 2**, **Figs. 2** and **3** and Online Methods). The 4.4-Å reconstruction represents the dominant class (49% of particles sorted by 3D classification; **Supplementary Fig. 4**). It reveals a hexamer with a right-handed spiral arrangement of subunits with an ~5-Å rise and ~60° twist per protomer (**Fig. 2**) that results in an ~30-Å offset between the first and last protomers (hereafter called P1 and P6) and an ~40-Å-wide gate between them (**Figs. 1f** and **2**). Notably, the microtubule-severing enzyme spastin and other AAA ATPases were proposed to form functional helical assemblies during their mechanochemical cycles on the basis of their propensities to form helical arrangements in crystals²⁵. Both katanin and spastin form helices in crystals (**Supplementary Fig. 5**) that are left-handed and much more open (~13–16-Å rise and ~60° twist per crystallographic copy) than the right-handed spiral arrangement we see in our cryo-EM reconstruction, thus resulting in a larger opening between the boundary

Table 2 Cryo-EM data collection, refinement and validation statistics

	Spiral conformation (EMD-8794, PDB 5WCO)	Ring Conformation (EMD-8796, PDB 5WCB)
Data collection		
Microscope	FEI Titan Krios	
Camera	Gatan K2 Summit	
Magnification	22,500	
Voltage (kV)	300	
Electron dose (e ⁻ /Å ²)	51	
Defocus range (μm)	–1.0 to –3.5	
Pixel size (Å)	1.31	
Reconstruction and refinement		
Particles	38,072	16,185
Map sharpening B factor (Å ²)	–98.36	–95.45
Resolution (Å)	4.4	6.0
FSC _{average}	0.884	0.90
Model composition		
Non-hydrogen atoms	11,477	11,422
Protein residues	1,660	1,662
Ligands (ATP)	6	5
R.m.s. deviations		
Bond lengths (Å)	0.003	0.004
Bond angles (°)	0.74	0.83
Validation		
MolProbity score	1.77	2.18
Clashscore	3.91	6.76
Poor rotamers (%)	0.00	0.00
Ramachandran plot		
Favored (%)	92.57	87.86
Allowed (%)	7.37	12.14
Disallowed (%)	0.06	0.00

subunits (~75 Å), consistent with the more limited crystal-packing interactions between the AAA domains. The second conformation identified by our cryo-EM analysis (24% of particles sorted by 3D classification) reveals a planar ring arrangement of the protomers that results in the closure of the gate between P1 and P6 (**Fig. 3** and **Supplementary Fig. 4**).

The cryo-EM reconstructions lack density for the MIT domains and the N-terminal half of the linker (**Fig. 1d**), thereby suggesting that these parts of katanin are flexible and thus averaged during image processing, consistent with our SAXS analyses that show a large distribution of angles for the arms protruding from the AAA ring (**Fig. 1** and **Supplementary Fig. 1**). The dimensions of the AAA ring in the cryo-EM reconstructions are consistent with those obtained from our low-resolution SAXS envelopes (**Fig. 1**). The C-terminal ends of the linkers that immediately precede the $\alpha 1$ helices (**Fig. 1d,f**, dark blue) form fishhook-shaped structures (**Fig. 1d,f**, light blue). The fishhooks and the $\alpha 1$ helices crown the N-terminal entry to a 20-Å-wide axial pore that opens up into the 40-Å-wide gate between P1 and P6 formed as the result of the spiral offset between the protomers (**Fig. 1f**). Well-defined density reveals a spiral arrangement of the pore loops 1 and 2, which are essential for the severing activities of katanin and spastin^{23,26}. These loops are poorly ordered in the monomer katanin X-ray structure (**Fig. 1e**), indicating that they are stabilized upon hexamerization. Pore loop 1 contains a conserved aromatic residue characteristic of all AAA ATPase polypeptide unfoldases that is critical for direct interaction and translocation of the

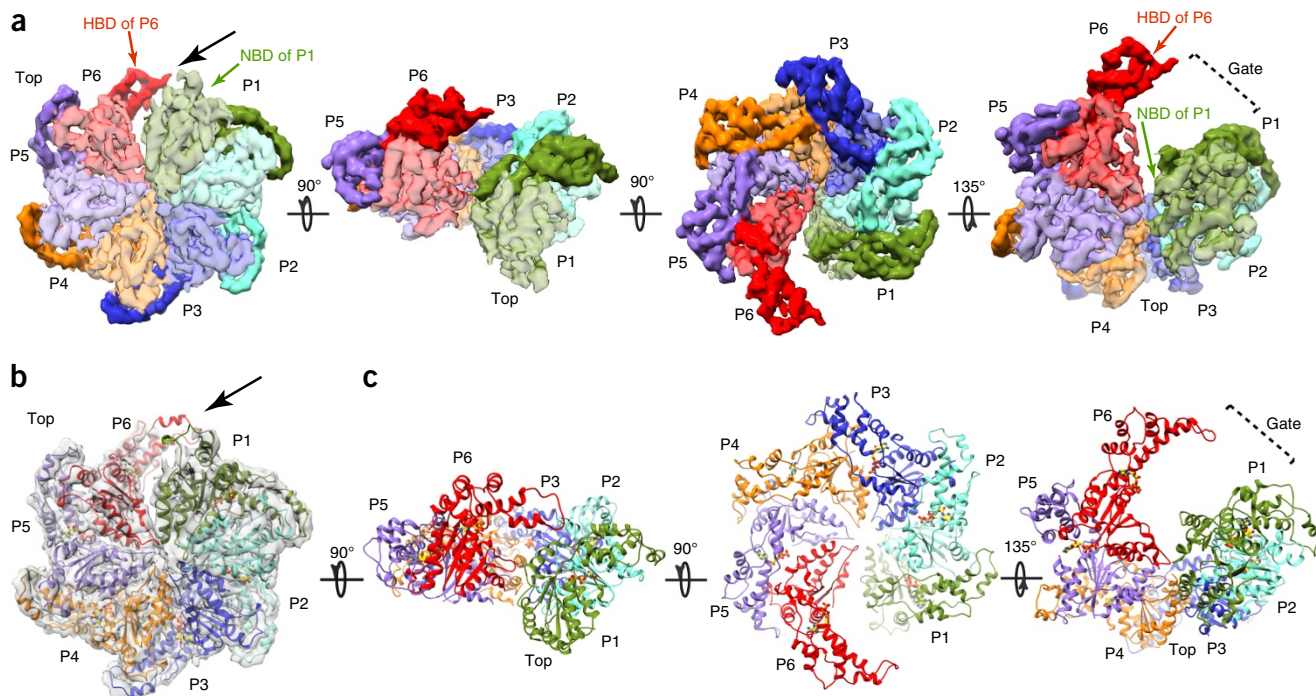


Figure 2 Cryo-EM maps and 3D models for the katanin hexamer in the spiral conformation. **(a)** Views of the katanin spiral conformation (rotation angles between the different views indicated with arrows). Protomer P1, green; P2, cyan; P3, blue; P4, orange; P5, purple; P6, red. NBD, HBD, light and dark hues, respectively. Black arrow indicates the open gate between protomers P1 and P6. **(b)** Top view of the spiral conformation with fitted atomic model. Cryo-EM map is shown as a transparent gray isosurface. The resolution of the map precluded *de novo* building of the fishhook linker element. Protomer color scheme same as in **a**. **(c)** Views of the atomic models for the katanin spiral conformation in the orientations shown above in **a**.

substrate, whereas pore loop 2 consists of positively charged residues that are highly conserved among severing enzymes (**Supplementary Fig. 2** and ref. 23).

The NBD and HBD of the AAA core of each protomer form two lobes of a crescent. Protomers P2 through P5 make canonical convex-to-concave AAA interactions between successive protomers^{27–29} (**Fig. 2a**). For a given protomer, the convex face of its NBD interacts with both the NBD and HBD of one neighboring protomer, whereas its concave face interacts with the NBD of the other neighbor. In the spiral arrangement, the gate is opened by the loss of convex and concave interactions for P1 and P6, respectively (**Fig. 2**). In the ring conformation, protomers P2 through P5 retain their helical arrangement ($\sim 5\text{-}\text{\AA}$ rise and $\sim 60^\circ$ twist per protomer as for P1 through P6 in the spiral conformation) with the canonical AAA-ring interactions (**Fig. 3**). However, because of a 44° rotation, the P1 NBD makes near-canonical interactions with the HBD in P6 and noncanonical interactions on both its convex and concave interfaces with the NBDs of P6 and P2, respectively, thus closing the P1–P6 gate (**Fig. 3**).

Katanin hexameric assembly is mediated by elements unique to microtubule-severing enzymes

Katanin augments the canonical AAA mode of interprotomer association with interactions mediated by structural elements characteristic to microtubule-severing enzymes: the fishhook-shaped linker element, helix $\alpha 1$ and helix $\alpha 12$ (**Fig. 1d,f** and **Supplementary Fig. 2**). Helix $\alpha 1$ (**Fig. 1f**, dark blue) of the concave face of the NBD of one protomer makes contacts with the linker that crowns the NBD of the neighboring protomer (**Fig. 1f**). Additional contacts are mediated by the $\alpha 1$ – $\alpha 2$ and $\alpha 5$ – $\beta 4$ loops that are positioned to sense conformational changes in the nucleotide-binding pocket and become ordered upon ATP-dependent hexamer formation (**Supplementary Fig. 6a**). Notably, mutation of

conserved Ile195 to lysine in the $\alpha 1$ – $\alpha 2$ loop inactivates katanin in *C. elegans*^{30,31}. $\alpha 12$ helices form part of a belt around the C-terminal side of the axial channel (**Fig. 1f**, orange). This arrangement is mediated by a tight interaction between the conserved $\alpha 11$ – $\alpha 12$ linker of one protomer and the four C-terminal residues of the adjacent protomer that immediately follow helix $\alpha 12$ (**Supplementary Fig. 6b**). These four terminal residues are highly conserved among microtubule-severing enzymes and are disordered in the monomeric crystal structures of both katanin (**Fig. 1e**) and spastin^{23,25}, consistently with their role in hexamer assembly. These residues include invariant Phe469 and Gly470 (**Supplementary Figs. 2** and **6b**). Mutation of Gly470 to aspartate impairs katanin activity in *C. elegans*^{30,31}, whereas mutation of Phe469 impairs both ATPase and microtubule-severing activity of katanin *in vitro* (**Supplementary Table 1** and Online Methods). Mutation of the equivalent aromatic residue in spastin also has a drastic effect on microtubule-severing activity²³.

Nucleotide state of a gating subunit mediates conformational transition in katanin hexamer

In the spiral conformation, all nucleotide-binding sites are occupied by ATP (**Fig. 4**), with clear density visible for all three phosphates as indicated by difference map analysis between the cryo-EM map and the nucleotide-free atomic model (**Fig. 4c–e**, **Supplementary Fig. 7a,c**). ATP binds at the NBD–HBD junction (**Fig. 4a**). Accordingly, the angle between the NBD and HBD is similar in all six protomers (C α r.m.s. deviation $\sim 0.3\text{ \AA}$; **Fig. 4a**). AAA ATPases contain arginine residues at the interprotomer interface termed ‘arginine fingers’ that stimulate hydrolysis of ATP *in trans* around their rings³². In katanin, invariant Arg351 and Arg352 from protomers P2 through P6 are $\sim 4\text{ \AA}$ away from the ATP β - and γ -phosphates of the neighboring protomer, yielding a catalytically competent arrangement of the nucleotide-binding

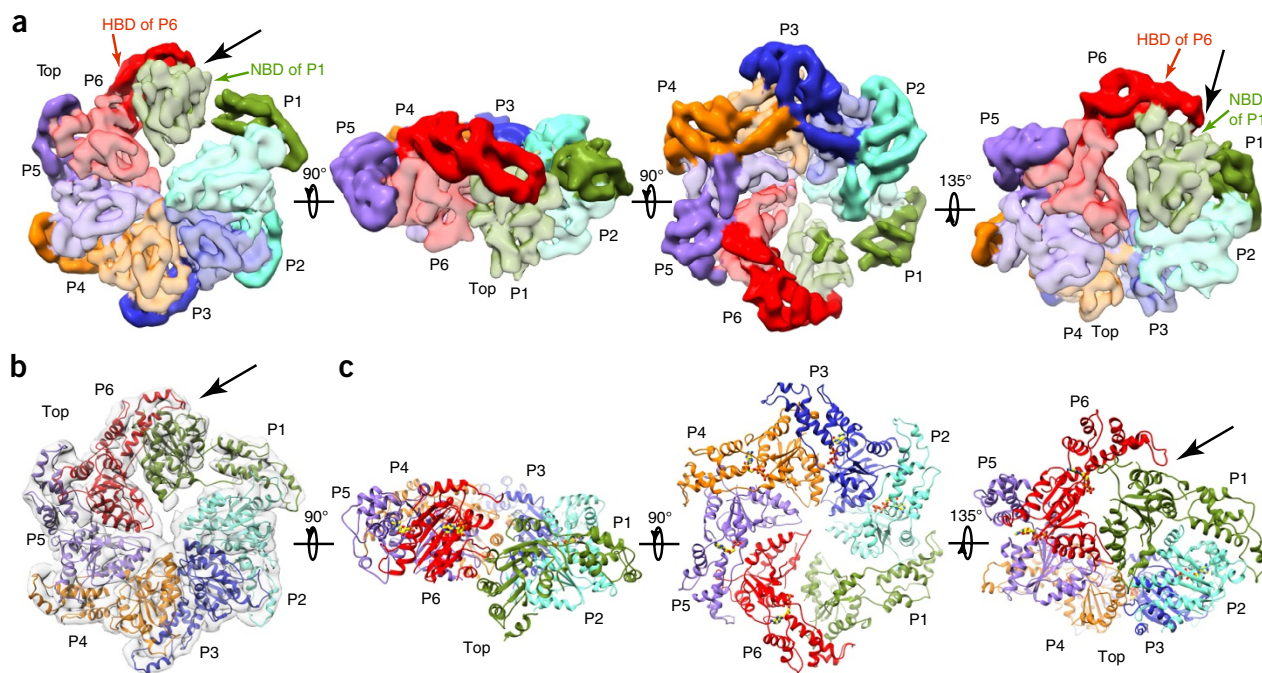


Figure 3 Cryo-EM maps and 3D models for the katanin hexamer in the ring conformation. (a) Views of the katanin ring conformation (rotation angles between the different views indicated with arrows). Protomer P1, green; P2, cyan; P3, blue; P4, orange; P5, purple; P6, red. NBD and HBD are shown in light and dark hue, respectively. Black arrows indicate the newly formed P1–P6 interface. (b) Top view of the ring conformation with fitted atomic model. Cryo-EM map, shown as a transparent gray isosurface. Protomers colored as in a. (c) Views of the atomic models for the katanin ring conformation in the orientations shown above in a.

pockets in protomers P1 through P5 (Fig. 5a,b and Supplementary Fig. 6c). The exception is protomer P6 where the ATP is ~36 Å from the arginine fingers in P1 (Fig. 5c). Mutation of both Arg351 and Arg352 drastically reduces katanin ATPase and inactivates microtubule severing (Supplementary Table 1).

In the ring conformation, no nucleotide density is visible in the P1 protomer (Fig. 4h,i and Supplementary Fig. 7b). Protomers P2 through P6 have bound ATP (Fig. 4j and Supplementary Fig. 7b,d). Consistent with the absence of ATP at the P1–P2 interface, the arginine fingers that would be supplied *in trans* by P2 are ~12 Å from the nucleotide-binding pocket (Fig. 5b,e). The loss of ATP in P1 widens the angle between the NBD and HBD by ~18° (Fig. 4f). As a result, the P1–P2 interface relaxes. It loses NBD–NBD contacts and the interface is formed only by interactions between the P1 HBD and P2 NBD (Fig. 3a,b). As a result, the salt bridge between invariant Arg244 in P1 and invariant Asp322 in P2 present in the spiral conformation (Fig. 5b) is lost (Fig. 5e). Consistent with its importance, mutation of Asp322 reduces ATPase by 96% and inactivates katanin in *in vitro* microtubule-severing assays (Supplementary Table 1). The rotation of the P1 NBD brings it into contact with P6, thereby closing the gate (Figs. 3 and 5f and Supplementary Video 1). In the canonical interface, helix $\alpha 5$ is involved in extensive interprotomer interactions, notably with the Walker B motif that senses nucleotide identity, whereas helix $\alpha 1$ makes contact with the fishhook-shaped linker element of the neighboring protomer (Figs. 5a,b,d and 1f). The loss of nucleotide in P1 displaces $\alpha 5$ so that it packs against $\alpha 1$ in P6 and makes more limited interprotomer contacts (Fig. 5f). Notably, mutations of residues in helix $\alpha 5$ of spastin are found in hereditary spastic paraplegia cases and impair microtubule-severing activity (Supplementary Fig. 2 and refs. 23,33).

DISCUSSION

AAA proteins actively thread their substrate biopolymers through an axial channel with the help of conserved pore loops, thus leading to remodeling or disassembly of their substrates³⁴. Katanin and spastin are thought to sever the microtubule by engaging the C-terminal tails of tubulin with their essential pore loops and pulling on them to dislodge tubulin subunits out of the microtubule lattice^{23,35}. The lack of structural information on microtubule-severing enzymes has, however, impeded the advancement of a mechanistic framework for the mechanochemical cycle for this class of enzymes. The spiral and ring conformations of the katanin AAA motor that we uncovered in our study suggest a power stroke that links ATP hydrolysis and nucleotide release to microtubule severing. The katanin hexamer binds the tubulin tails that are essential for severing^{18,35–38}. In the spiral ATP-bound conformation, the pore loops stack sequentially to form a spiral ladder optimal for substrate translocation, with pore loop 1 of protomer P1 positioned at the bottom of the spiral close to the microtubule-binding surface and the open gate between P1 and P6 facilitating access of the tubulin C-terminal tail to the axial pore. Moreover, the NBD of P1 is exposed in this conformation and accessible to the tubulin tail, which may thus directly stimulate its ATPase upon binding. Our structure reveals that the novel linker element, pore loops 1 and 2, and helix $\alpha 12$ form a contiguous interface through the axial channel that is optimal for substrate binding and translocation (Fig. 1f and Supplementary Video 1). The location of the fishhook linker element indicates that it is likely one of the first structural elements to interact with the microtubule surface. This structural element is absent in vacuolar protein sorting-associated protein 4 (Vps4), which together with katanin, spastin and fidgetin forms the meiotic clade of AAA ATPases^{39,40}. Thus, the fishhook linker is a distinguishing

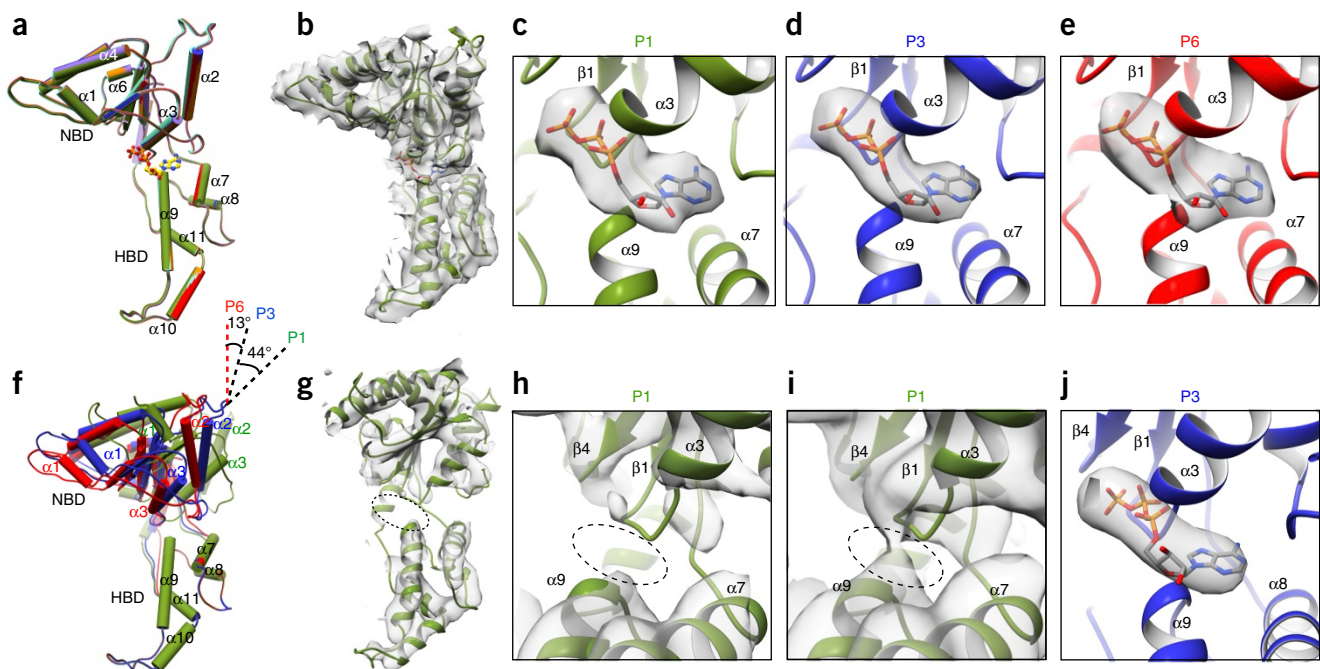


Figure 4 Different nucleotide occupancies in the spiral and ring conformations of the katanin hexamer. **(a)** Superposition of protomers P1 through P6 in the spiral conformation. (C α overall r.m.s. deviation \sim 0.3 Å.) Protomer scheme is same as in **Figure 2a**. **(b)** P1 structure in the spiral conformation. Bound ATP shown as stick representation. **(c–e)** Enlarged views of the nucleotide-binding pocket showing bound ATP for protomers P1, P3 and P6 in the spiral conformation with the difference map as transparent gray isosurface (**Supplementary Fig. 7a,c** and Online Methods). **(f)** Superposition of P1, P3 and P6 in the ring conformation showing the 44° rotation of the NBD in the P1 protomer. **(g)** P1 structure in the ring conformation. Dotted oval indicates ATP-binding region. **(h,i)** Enlarged views of the nucleotide-binding pocket at two contour levels, 15 σ (**h**) and 10 σ (**i**), showing the absence of nucleotide in P1. **(j)** Enlarged view of the nucleotide-binding pocket showing bound ATP for protomer P3 in the ring conformation with the difference map as transparent gray isosurface (**Supplementary Fig. 7b,d**).

feature of katanin. Interestingly, linker residue Ser135, immediately proximal to the fishhook element, is phosphorylated by Aurora B kinase. This phosphorylation impairs katanin microtubule-stimulated ATPase and severing, thus positively regulating spindle size in *Xenopus laevis*^{9,41}. The additional negative charges proximal to the channel entrance likely interfere with the productive engagement of the negatively charged microtubule substrate. In spastin, mutations of residues in this region or deletion of this linker element impair microtubule severing^{23,35}.

We propose that ATP hydrolysis and nucleotide release in P1 drives the transition to the ring state, thus displacing the linker and pore loop in P1 by \sim 20 Å together with the bound tubulin substrate (**Fig. 6a,b** and **Supplementary Video 1**) from the bottom of the spiral and up into the axial channel of the hexamer. The tubulin chain can be then further pulled into the axial channel by the engagement of loop 1 in protomer P2 for another cycle through a sequential mechanism of ATP hydrolysis in the AAA ring. This \sim 20-Å displacement would correspond to an approximately 5-amino-acid-length translocation of the C-terminal tubulin tail from the microtubule surface toward the center of the axial pore.

The katanin MIT domain binds the microtubule autonomously with low affinity⁴². Our SAXS analyses of the katanin hexamer demonstrate that the MIT domains are located at the tip of flexible arms that connect them to the AAA core. This flexibility is likely important to the ability of the MIT domains and the AAA ring to simultaneously engage the microtubule substrate through multivalent interactions and thus help the enzyme stay anchored to the microtubule as it remodels its AAA ring during the mechanochemical cycle and pulls on the tubulin tails with its pore loops (**Fig. 6c**). The avidity-based

interaction with the microtubule through the MIT domains could also help retain the assembled enzyme on the polymer for subsequent engagement of neighboring tubulin tails if the extraction of one tubulin subunit is not enough to initiate catastrophic breakdown of the microtubule lattice. Complete unfolding and axial translocation of the entire polypeptide chain as in the case of ClpX or Vps4 (refs. 43,44) is not absolutely necessary as the microtubule could be destabilized by repeated ‘tugging’ on the tubulin to apply a distorting force to the protofilament structure by cycling through the spiral and closed-ring states in a mechanism more analogous to the one recently proposed for NSF⁴⁵.

In addition to our results on microtubule severing, recent structural studies of AAA ATPases that remodel protein complexes or aggregates such as Hsp104 (ref. 46), ClpX (ref. 29), the archaeal homolog of p97 of unknown function, VAT⁴⁷, the proteasome^{48,49} and Vps4 (refs. 39,40) have identified asymmetric spiral architectures of AAA rings with pore loops stacked in a spiral suggestive of a relay of the substrate through their central pores. Recent cryo-EM studies identified both open and closed spiral configurations for VAT and Vps4 in the presence of substrate and as a function of nucleotide state^{40,47}, thereby suggesting a mechanism analogous to katanin, although there are differences in nucleotide occupancies between these structures, consistent with their different domain organization and function. The substrate-bound structures of Vps4 (ref. 40) and VAT⁴⁷ are asymmetric, with five of the pore loops bound to the unfolded substrate polypeptide and arranged in a tight spiral and the sixth subunit in a different conformation and disengaged from the substrate. Thus, a common theme is emerging for some AAA ATPases whereby the power stroke for substrate translocation is generated by breaking the

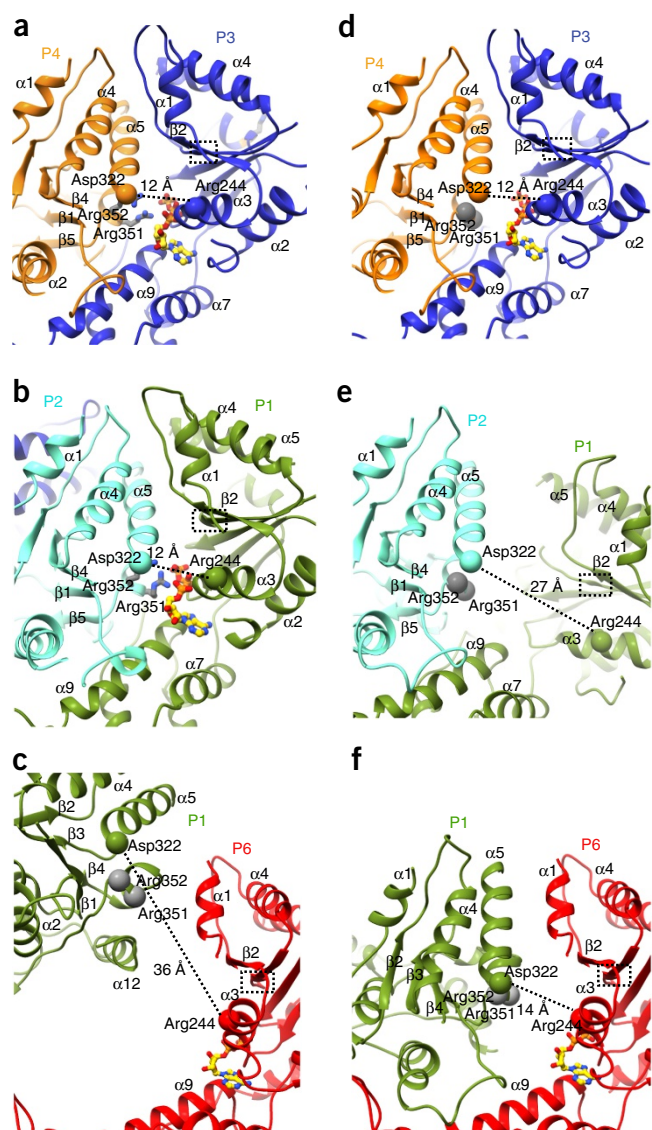


Figure 5 Protomer-protomer interface rearrangements between the spiral and ring conformations: transition between tense and relaxed states of the P1 gating protomer. **(a,b)** Canonical P3–P4 **(a)** and P1–P2 **(b)** interfaces in the spiral conformation highlighting the potential salt bridge between invariant Arg244 and Asp322 (C α shown as spheres). **(c)** Lack of contacts between the P6 and P1 protomers in the spiral conformation. **(d)** Canonical P3–P4 interface in the ring conformation highlighting the potential salt bridge between invariant Arg244 and Asp322 (C α shown as spheres). **(e)** The relaxed noncanonical P1–P2 interface in the ring conformation. **(f)** The P6–P1 interface in the ring conformation. The Walker B region is indicated by a dashed-line box in all panels, and arginine fingers are represented as gray ball and stick **(a,b)** or C α spheres **(c–f)**.

helical symmetry of a spiral arrangement of subunits by a boundary subunit in response to nucleotide hydrolysis. Such a mechanism for substrate translocation was originally advanced for nucleic acid AAA ATPase translocases such as the DNA helicase E1 (ref. 50) and the RNA translocase Rho^{51,52}. In contrast to these enzymes, the recent cryo-EM reconstructions of p97 show six-fold symmetric arrangements indicative of a concerted mechanism of substrate engagement and remodeling⁵³ and highlight the mechanistic richness used by AAA ATPases, consistent with their large representation in the genome and diverse cellular substrates and functions. Thus, details

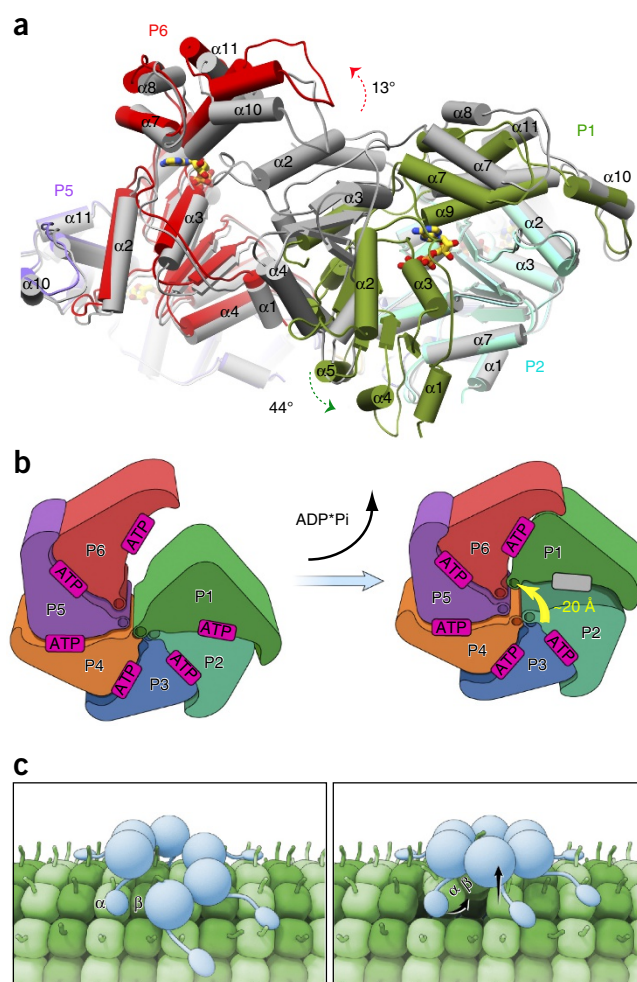


Figure 6 Pore loop displacement of the gating protomer suggests power stroke for microtubule severing. **(a)** Superposition of the katanin spiral and ring conformations shows the large movement of the gating protomer P1 (green arrow) and the smaller-scale movement of P6 (red arrow). Protomer color scheme same as in **Figure 2** in the spiral conformation; protomers are gray in the ring conformation. **(b)** Cartoon depicting the movement of protomer P1 between the spiral and ring conformations. Protomer color scheme same as in **Figure 2**. Yellow arrow indicates the translocation of loop 1 of the P1 gating protomer. **(c)** Cartoon illustrating the proposed power stroke that extracts a tubulin dimer and initiates microtubule-lattice breakdown and severing. Left, katanin (blue) assembles as a hexamer with a spiral configuration of the AAA domains and with the MIT domains emanating from the AAA motor core and making multivalent interactions with the microtubule (green). The flexible tubulin tail is engaged in the axial pore of the katanin hexamer. Right, ATP hydrolysis and release in the gating protomer P1 leads to closure of the AAA ring and a ~20-Å displacement in the P1 loop that translocates with it the bound C-terminal tail of a tubulin subunit. The cycle is repeated until lattice contacts unravel and the microtubule severs.

of nucleotide occupancies and nucleotide hydrolysis mechanism are likely different between AAA ATPases, and they might even differ between substrates for the same enzyme, as studies on ClpB and Hsp104 have shown different ATP hydrolysis mechanisms depending on the type of substrate they engage^{54,55}. This is an interesting aspect to consider when comparing microtubule-severing enzymes and other closely related AAA ATPases, as the former are able to disassemble one of the stiffest noncovalent polymer structures found in eukaryotic cells².

The mechanistic complexity of AAA ATPases highlights the importance of obtaining high-resolution structural and kinetic information for each enzyme along its entire mechanochemical cycle and with its physiological substrates. Future structures of katanin and spastin in different nucleotide-bound states and with the microtubule substrate will be critical for elucidating how these enzymes generate the force needed to disrupt lattice interfaces in the microtubule polymer that ultimately lead to its catastrophic disassembly. Our structural study is an important first step toward establishing a mechanistic framework for these fascinating molecular machines.

METHODS

Methods, including statements of data availability and any associated accession codes and references, are available in the [online version of the paper](#).

Note: Any Supplementary Information and Source Data files are available in the [online version of the paper](#).

ACKNOWLEDGMENTS

We are grateful to N. Grigorieff for initial advice and access to the Krios for collection of one high-resolution data set, R. Diaz-Avalos for data collection advice, J. Hinshaw and H. Wang for TF20 access and F. McNally (University of California, Davis) for a katanin expression plasmid. X-ray diffraction data were collected at beamline 502 of the Advanced Light Source, which is a DOE Office of Science User Facility under contract no. DE-AC02-05CH11231. SAXS was performed at Beamline 12ID-B of the Advanced Photon Source, which is a US DOE Office of Science User Facility operated for the DOE Office of Science by Argonne National Laboratory under Contract No. DE-AC02-06CH11357. A.R.-M. is supported by the intramural programs of NINDS and NHLBI.

AUTHOR CONTRIBUTIONS

E.Z. prepared grids, collected and processed EM data with input from A.R.-M. The high-resolution data set was collected at the Janelia Research Campus (Howard Hughes Medical Institute). All EM data were processed on the Biowulf cluster at the National Institutes of Health. A.R.-M. and E.Z. built and refined models. A.S. purified proteins, obtained crystals, collected X-ray diffraction and SAXS data and performed ATP-binding and ATP-hydrolysis assays. G.P. performed and interpreted AUC. E.W. performed *in vitro* severing assays. X.Z. collected and processed SAXS data. A.R.-M. refined X-ray structure. A.R.-M. and E.Z. wrote manuscript. All authors reviewed the manuscript. A.R.-M. conceived project and supervised research.

COMPETING FINANCIAL INTERESTS

The authors declare no competing financial interests.

Reprints and permissions information is available online at <http://www.nature.com/reprints/index.html>. Publisher's note: Springer Nature remains neutral with regard to jurisdictional claims in published maps and institutional affiliations.

- Roll-Mecak, A. & McNally, F.J. Microtubule-severing enzymes. *Curr. Opin. Cell Biol.* **22**, 96–103 (2010).
- Gittes, F., Mickey, B., Nettleton, J. & Howard, J. Flexural rigidity of microtubules and actin filaments measured from thermal fluctuations in shape. *J. Cell Biol.* **120**, 923–934 (1993).
- Ahmad, F.J., Yu, W., McNally, F.J. & Baas, P.W. An essential role for katanin in severing microtubules in the neuron. *J. Cell Biol.* **145**, 305–315 (1999).
- Yu, W. *et al.* The microtubule-severing proteins spastin and katanin participate differently in the formation of axonal branches. *Mol. Biol. Cell* **19**, 1485–1498 (2008).
- Zhang, Q., Fishel, E., Bertrache, T. & Dixit, R. Microtubule severing at crossover sites by katanin generates ordered cortical microtubule arrays in *Arabidopsis*. *Curr. Biol.* **23**, 2191–2195 (2013).
- Lindeboom, J.J. *et al.* A mechanism for reorientation of cortical microtubule arrays driven by microtubule severing. *Science* **342**, 1245533 (2013).
- McNally, K., Audhya, A., Oegema, K. & McNally, F.J. Katanin controls mitotic and meiotic spindle length. *J. Cell Biol.* **175**, 881–891 (2006).
- Cummings, C.M., Bentley, C.A., Perdue, S.A., Baas, P.W. & Singer, J.D. The Cul3/Klhd5 E3 ligase regulates p60/katanin and is required for normal mitosis in mammalian cells. *J. Biol. Chem.* **284**, 11663–11675 (2009).
- Loughlin, R., Wilbur, J.D., McNally, F.J., Nédélec, F.J. & Heald, R. Katanin contributes to interspecies spindle length scaling in *Xenopus*. *Cell* **147**, 1397–1407 (2011).
- McNally, K. *et al.* Katanin maintains meiotic metaphase chromosome alignment and spindle structure *in vivo* and has multiple effects on microtubules *in vitro*. *Mol. Biol. Cell* **25**, 1037–1049 (2014).
- Srayko, M., O'toole, E.T., Hyman, A.A. & Müller-Reichert, T. Katanin disrupts the microtubule lattice and increases polymer number in *C. elegans* meiosis. *Curr. Biol.* **16**, 1944–1949 (2006).
- Zhang, D., Rogers, G.C., Buster, D.W. & Sharp, D.J. Three microtubule severing enzymes contribute to the "Pacman-flux" machinery that moves chromosomes. *J. Cell Biol.* **177**, 231–242 (2007).
- Sharma, N. *et al.* Katanin regulates dynamics of microtubules and biogenesis of motile cilia. *J. Cell Biol.* **178**, 1065–1079 (2007).
- Hu, W.F. *et al.* Katanin p80 regulates human cortical development by limiting centriole and cilia number. *Neuron* **84**, 1240–1257 (2014).
- Mishra-Gorur, K. *et al.* Mutations in KATNB1 cause complex cerebral malformations by disrupting asymmetrically dividing neural progenitors. *Neuron* **84**, 1226–1239 (2014).
- Yigit, G. *et al.* A syndrome of microcephaly, short stature, polysyndactyly, and dental anomalies caused by a homozygous KATNB1 mutation. *Am. J. Med. Genet. A.* **170**, 728–733 (2016).
- Vale, R.D. Severing of stable microtubules by a mitotically activated protein in *Xenopus* egg extracts. *Cell* **64**, 827–839 (1991).
- McNally, F.J. & Vale, R.D. Identification of katanin, an ATPase that severs and disassembles stable microtubules. *Cell* **75**, 419–429 (1993).
- Hartman, J.J. *et al.* Katanin, a microtubule-severing protein, is a novel AAA ATPase that targets to the centrosome using a WD40-containing subunit. *Cell* **93**, 277–287 (1998).
- McNally, F.J., Okawa, K., Iwamatsu, A. & Vale, R.D. Katanin, the microtubule-severing ATPase, is concentrated at centrosomes. *J. Cell Sci.* **109**, 561–567 (1996).
- Joly, N., Martino, L., Gigant, E., Dumont, J. & Pintard, L. Microtubule-severing activity of AAA+ ATPase Katanin is essential for female meiotic spindle assembly. *Development* **143**, 3604–3614 (2016).
- Hartman, J.J. & Vale, R.D. Microtubule disassembly by ATP-dependent oligomerization of the AAA enzyme katanin. *Science* **286**, 782–785 (1999).
- Roll-Mecak, A. & Vale, R.D. Structural basis of microtubule severing by the hereditary spastic paraplegia protein spastin. *Nature* **451**, 363–367 (2008).
- Scott, A. *et al.* Structural and mechanistic studies of VPS4 proteins. *EMBO J.* **24**, 3658–3669 (2005).
- Taylor, J.L., White, S.R., Lauring, B. & Kull, F.J. Crystal structure of the human spastin AAA domain. *J. Struct. Biol.* **179**, 133–137 (2012).
- Johjima, A. *et al.* Microtubule severing by katanin p60 AAA+ ATPase requires the C-terminal acidic tails of both α - and β -tubulins and basic amino acid residues in the AAA+ ring pore. *J. Biol. Chem.* **290**, 11762–11770 (2015).
- Caillat, C. *et al.* Asymmetric ring structure of Vps4 required for ESCRT-III disassembly. *Nat. Commun.* **6**, 8781 (2015).
- Lenzen, C.U., Steinmann, D., Whiteheart, S.W. & Weis, W.I. Crystal structure of the hexamerization domain of N-ethylmaleimide-sensitive fusion protein. *Cell* **94**, 525–536 (1998).
- Glynn, S.E., Martin, A., Nager, A.R., Baker, T.A. & Sauer, R.T. Structures of asymmetric ClpX hexamers reveal nucleotide-dependent motions in a AAA+ protein-unfolding machine. *Cell* **139**, 744–756 (2009).
- Mains, P.E., Kempfues, K.J., Sprunger, S.A., Sulston, I.A. & Wood, W.B. Mutations affecting the meiotic and mitotic divisions of the early *Caenorhabditis elegans* embryo. *Genetics* **126**, 593–605 (1990).
- Clark-Maguire, S. & Mains, P.E. mei-1, a gene required for meiotic spindle formation in *Caenorhabditis elegans*, is a member of a family of ATPases. *Genetics* **136**, 533–546 (1994).
- Wendler, P., Ciniawsky, S., Kock, M. & Kube, S. Structure and function of the AAA+ nucleotide binding pocket. *Biochim. Biophys. Acta* **1823**, 2–14 (2012).
- Fonknechten, N. *et al.* Spectrum of SPG4 mutations in autosomal dominant spastic paraplegia. *Hum. Mol. Genet.* **9**, 637–644 (2000).
- Hanson, P.I. & Whiteheart, S.W. AAA+ proteins: have engine, will work. *Nat. Rev. Mol. Cell Biol.* **6**, 519–529 (2005).
- White, S.R., Evans, K.J., Lary, J., Cole, J.L. & Lauring, B. Recognition of C-terminal amino acids in tubulin by pore loops in Spastin is important for microtubule severing. *J. Cell Biol.* **176**, 995–1005 (2007).
- Roll-Mecak, A. & Vale, R.D. The *Drosophila* homologue of the hereditary spastic paraplegia protein, spastin, severs and disassembles microtubules. *Curr. Biol.* **15**, 650–655 (2005).
- Valenstein, M.L. & Roll-Mecak, A. Graded control of microtubule severing by tubulin glutamylation. *Cell* **164**, 911–921 (2016).
- Bailey, M.E., Sackett, D.L. & Ross, J.L. Katanin severing and binding microtubules are inhibited by tubulin carboxy tails. *Biophys. J.* **109**, 2546–2561 (2015).
- Su, M. *et al.* Mechanism of Vps4 hexamer function revealed by cryo-EM. *Sci. Adv.* **3**, e1700325 (2017).
- Monroe, N., Han, H., Shen, P.S., Sundquist, W.I. & Hill, C.P. Structural basis of protein translocation by the Vps4-Vta1 AAA ATPase. *eLife* **6**, e24487 (2017).
- Whitehead, E., Heald, R. & Wilbur, J.D. N-terminal phosphorylation of p60 katanin directly regulates microtubule severing. *J. Mol. Biol.* **425**, 214–221 (2013).
- Iwaya, N. *et al.* A common substrate recognition mode conserved between katanin p60 and VPS4 governs microtubule severing and membrane skeleton reorganization. *J. Biol. Chem.* **285**, 16822–16829 (2010).

43. Olivares, A.O., Nager, A.R., Iosefson, O., Sauer, R.T. & Baker, T.A. Mechanochemical basis of protein degradation by a double-ring AAA+ machine. *Nat. Struct. Mol. Biol.* **21**, 871–875 (2014).
44. Yang, B., Stjepanovic, G., Shen, Q., Martin, A. & Hurley, J.H. Vps4 disassembles an ESCRT-III filament by global unfolding and processive translocation. *Nat. Struct. Mol. Biol.* **22**, 492–498 (2015).
45. Zhao, M. *et al.* Mechanistic insights into the recycling machine of the SNARE complex. *Nature* **518**, 61–67 (2015).
46. Yokom, A.L. *et al.* Spiral architecture of the Hsp104 disaggregase reveals the basis for polypeptide translocation. *Nat. Struct. Mol. Biol.* **23**, 830–837 (2016).
47. Ripstein, Z.A., Huang, R., Augustyniak, R., Kay, L.E. & Rubinstein, J.L. Structure of a AAA+ unfoldase in the process of unfolding substrate. *eLife* **6**, e25754 (2017).
48. Lander, G.C. *et al.* Complete subunit architecture of the proteasome regulatory particle. *Nature* **482**, 186–191 (2012).
49. Wehmer, M. *et al.* Structural insights into the functional cycle of the ATPase module of the 26S proteasome. *Proc. Natl. Acad. Sci. USA* **114**, 1305–1310 (2017).
50. Enemark, E.J. & Joshua-Tor, L. Mechanism of DNA translocation in a replicative hexameric helicase. *Nature* **442**, 270–275 (2006).
51. Thomsen, N.D. & Berger, J.M. Running in reverse: the structural basis for translocation polarity in hexameric helicases. *Cell* **139**, 523–534 (2009).
52. Thomsen, N.D., Lawson, M.R., Witkowsky, L.B., Qu, S. & Berger, J.M. Molecular mechanisms of substrate-controlled ring dynamics and substepping in a nucleic acid-dependent hexameric motor. *Proc. Natl. Acad. Sci. USA* **113**, E7691–E7700 (2016).
53. Banerjee, S. *et al.* 2.3 Å resolution cryo-EM structure of human p97 and mechanism of allosteric inhibition. *Science* **351**, 871–875 (2016).
54. Doyle, S.M., Hoskins, J.R. & Wickner, S. DnaK chaperone-dependent disaggregation by caseinolytic peptidase B (ClpB) mutants reveals functional overlap in the N-terminal domain and nucleotide-binding domain-1 pore tyrosine. *J. Biol. Chem.* **287**, 28470–28479 (2012).
55. DeSantis, M.E. *et al.* Operational plasticity enables hsp104 to disaggregate diverse amyloid and nonamyloid clients. *Cell* **151**, 778–793 (2012).

ONLINE METHODS

Protein expression and purification. *C. elegans* katanin p60 was expressed in *Escherichia coli* as a maltose binding-fusion protein. Cultures were grown at 37 °C to an OD₆₀₀ of ~1.0 and katanin expression was induced with 0.5 mM IPTG at 16 °C and for 14 h. Harvested cells were resuspended in 50 mM HEPES, pH 7.5, 500 mM KCl, 10 mM MgCl₂, 1 mM DTT, and 1 mM PMSF and lysed with a microfluidizer in the presence of a protease-inhibitor cocktail (Roche). The supernatant was collected by centrifugation at 31,000 × *g* for 40 min and loaded onto amylose resin (New England Biolabs), equilibrated in 50 mM HEPES, pH 7.5, 500 mM KCl, 10 mM MgCl₂ and 1 mM DTT. Katanin was released from the resin by cleavage with Tobacco Etch Virus protease. Katanin was further purified by anion exchange chromatography. The sample was exchanged into buffer containing 20 mM HEPES, pH 7.5, 300 mM KCl, 10 mM MgCl₂, 1 mM TCEP and 15% glycerol and flash frozen in liquid nitrogen for storage at –80 °C. Prior to conducting all AUC, SAXS and EM analyses, katanin was further purified by size exclusion chromatography on a Superose 6 Increase 10/300 GL column (GE Healthcare). In order to determine the stoichiometry of ATP to the katanin hexamer, we chromatographed full-length and ΔMIT katanin p60 (100 μL of 100 μM) on a Superose 6 10/300 GL Increase column in the buffer containing excess ATP (100 μM). As the protein migrated through the gel filtration matrix, it depleted ATP from the buffer, resulting in a negative peak. Bound ATP was determined from the area of the negative ATP-depletion peak. The determined molar ratio of ATP per katanin hexamer was 5.6 ± 0.3 (*n* = 3 independent experiments). Mutants were generated using Quickchange (Stratagene).

Analytical ultracentrifugation. AUC experiments were conducted at 24, 12, 6 and 3 μM of katanin p60 concentrations in 20 mM HEPES, pH 7.5, 300 mM KCl, 10 mM MgCl₂, and 1 mM TCEP with or without 100 μM ATP. Measurements were collected in a ProteomeLab XL-I analytical ultracentrifuge (Beckman Coulter, Indianapolis, IN) using absorption optics. To obtain a final sample optical density in the 0.25 to 1.00 range, cells of 3-mm or 12-mm optical path length were used. Loaded cells, placed in the four-hole AN-Ti rotor, were thermally equilibrated in the ultracentrifuge. After thermal equilibrium was reached at rest at 10 °C or 20 °C, the rotor was accelerated to 45,000 r.p.m. to start the collection of intensity scans at 280 nm. The data were collected until no further sedimentation boundary movement was observed. Sedimentation velocity data analyses were performed with the program SEDFIT using a continuous *c*(*s*) model⁵⁶. All accepted fits have root-mean-r.m.s. deviations less than 0.008. Partial specific volume and buffer parameters were calculated with SEDNTERP (<http://www.jphilo.mailway.com>). Sedimentation coefficient distribution values were corrected to standard conditions of water at 20 °C, *s*_{20,w}.

Crystallization and X-ray structure determination. For crystallization, katanin p60 (E293Q) eluted from the size exclusion column (as described above) was supplemented with 1 mM ATP and concentrated to 10 mg/ml. Crystals grew by hanging-drop vapor diffusion at room temperature from protein mixed 2:1 (v/v) with the crystallization solution containing 1.0 M ammonium sulfate and 0.1 M Tris, pH 7.8. Crystals were cryoprotected with 25% glycerol before flash freezing in liquid nitrogen. X-ray diffraction data were collected at the Advanced Light Source, beamline 5.0.2. Crystals grew with the symmetry of space group *P*6₅ with one katanin protomer per asymmetric unit. Most crystals diffracted poorly and were not suitable for structural determination. Diffraction data were reduced with HKL2000 (ref. 57). Details of the experimental data collection and processing statistics are in **Table 1**. The structure was solved by molecular replacement using PHASER⁵⁸ with the previously published structure of spastin as the search model (PDB 3B9P, ref. 23). Multiple rounds of model building and refinement were performed with COOT⁵⁹ and PHENIX⁶⁰. The current refinement model for katanin p60 consists of 262 residues and one sulfate ion. Despite the presence of ATP in the crystallization conditions, no well-ordered nucleotide is visible in the maps. Six regions of the polypeptide chain (residues 1–172, 186–190, 263–269, 297–306, 324–332, 467–472) are not well resolved and presumed disordered. Residues 173–183, 270–284 and 310–322 were built as polyalanine, as the sequence register is based on the sequence alignment of the spastin X-ray structure. The fishhook element visible in the cryo-EM map is also visible in the X-ray model, although less well defined in the latter because of the lack of stabilization by protomer-protomer contacts. The quality of the map in this region was not sufficient to allow confident *de novo* building in either the X-ray or cryo-EM map. This structural

feature comprises ~25 residues N-terminal to helix α1. The current crystallographic model of the katanin protomer at 3.3-Å resolution has *R*_{work} and *R*_{free} of 30.8% and 24.8%, respectively (**Table 1**) with 91.1% of residues in favored regions and 1.0% in disallowed regions. The maximum-likelihood-based coordinate error is 0.53 Å. Figures were prepared with UCSF Chimera⁶¹.

Solution small-angle X-ray scattering. Solution SAXS experiments of full-length and ΔMIT katanin p60 (E293Q) were performed at beamline 12-ID-B of the Advanced Photon Source at Argonne National Laboratory using an in-line FPLC AKTA micro setup with a Superose 6 Increase 10/300 GL size exclusion column. The wavelength, λ, of X-ray radiation was set to 0.886 Å. Scattered X-ray intensities were measured using a Pilatus 2M detector. The sample-to-detector distance was set such that the detecting range of momentum transfer *q* (equal to 4π sinθ/λ, where 2θ is the scattering angle) was 0.004–0.55 Å^{–1}. The sample passed through the FPLC column and was fed to a flow cell for SAXS measurements. The flow cell is a cylindrical quartz capillary 1.5 mm in diameter with 10 μm wall thickness and is equipped with a Peltier cooling device that keeps the flow cell at 10 °C. SAXS data were collected at the elution peak while background data were collected before and after the peak. The exposure time was set to <1 s to reduce radiation damage. More than forty images were acquired for each sample (around the elution peak) and background in order to obtain good signal-to-noise ratio values. The 2D-scattering images were converted to 1D SAXS (*I*(*q*) vs. *q*) curves through azimuthally averaging after solid angle correction and then normalizing with the intensity of the transmitted X-ray beam flux, using custom scripts. The sample concentration was ~2.0–4.0 mg/ml at the elution peak. The SAXS profile of the protein was obtained by subtracting background from the sample data. The radius of gyration (*R*_g) was calculated using the Guinier equation⁶², $I(q) = I_0 \exp(-R_g^2 q^2 / 3)$ where *I*₀ is the forward scattering, an indicator of molecular weight⁶³. The pair distance distribution function *P*(*r*) that is the inverse Fourier transform of X-ray scattering data and roughly a weighted histogram of atomic-pair distances in the molecule, was calculated using GNOM v4.6 (ref. 64). *R*_g were calculated from the second momentum of the *P*(*r*) function and compared favorably to the initial value derived from the Guinier plots (**Supplementary Fig. 1e**), 67.7 ± 0.4 Å versus 63 ± 5 Å for full-length katanin p60 and 51.4 ± 0.3 Å versus 51 ± 1 Å for ΔMIT katanin p60. Molecular weights were estimated directly from the background-subtracted SAXS data using the program SCATTER v2.3h (ref. 65) and were 360 kDa and 260 kDa for katanin p60 and ΔMIT katanin p60, respectively. The expected molecular weights of the katanin p60 and ΔMIT katanin hexamers are 319 kDa and 252 kDa, respectively. 3D molecular envelopes were calculated from SAXS data up to *q* of 0.30 Å^{–1}, using DAMMIF v1.1.2, a fast version of DAMMIN⁶⁶. Twenty and twenty-four runs were performed for katanin p60 full-length and the ΔMIT construct, respectively. The reconstructions were aligned, averaged and filtered on the basis of occupancy using DAMAVER v5.0 (ref. 67). *P*6 symmetry was applied in the DAMMIF and DAMAVER calculations. The overall size of the DAMAVER averaged bead model was significantly reduced comparing to the individuals, indicating that the regions beyond the central ring have a high degree of flexibility (**Fig. 1a** and **Supplementary Fig. 1f,d,h**). Therefore, both the individual and averaged models are reported, with the former being a better representation of molecular size.

Cryo-electron microscopy specimen preparation, data acquisition and analysis. Katanin p60 (E293Q) was diluted to 0.6 mg/ml in 20 mM HEPES-KOH, pH 7.5, 300 mM KCl, 10 mM MgCl₂, 1 mM TCEP and 1 mM ATP and spun at 69,800 × *g* for 15 min at 4 °C. 5 μl was applied to a glow-discharged C-flat holey carbon grid with 1.2 μm hole, 1.3 μm space (C-flat, Electron Microscopy Sciences). The grids were blotted for 5 s at 90% humidity and plunge-frozen in liquid ethane cooled by liquid nitrogen using Leica EM GP (Leica Microsystems). To assess sample stability and monodispersity, cryo-EM data were first collected on a Tecnai TF20 electron microscope (FEI) operated at 200kV, equipped with a K2 Summit direct electron detector camera (Gatan) operated in electron counting mode. To obtain a preliminary reconstruction, ~800 images were recorded at a nominal magnification of 29,000×, corresponding to a physical pixel size of 1.27 Å/pixel. Images were recorded with a defocus range from –1.5 μm to –3.5 μm. With no specimen present, the rate of exposure of the detector was 6 e[–]/Å²/s. Exposure-fractionated movie stacks of 40 frames were recorded for 10 s with a total electron dose of 60 e[–]/Å².

To obtain a preliminary reconstruction of katanin p60 (E293Q), images were aligned with each other using Unblur⁶⁸. Defocus parameters were estimated from aligned sums of 5 frames using CTFFIND4 (ref. 69). 90,000 particles were manually picked from movie sums with the total dose of $60 \text{ e}^-/\text{\AA}^2$ and extracted in Relion using a 300-pixel box size⁷⁰. Images were downsampled to a pixel size of 2.54 Å and classified in 2D using Relion. An initial 3D reconstruction with C6 symmetry was generated using a subset of particles (40,000 particles) in FREALIGN⁷¹, following a protocol described previously⁷². To obtain the initial reconstruction, images were downsampled to 5.08 Å/pixel, and frequencies only up to $1/40 \text{ \AA}^{-1}$ in the initial rounds and up to $1/15 \text{ \AA}^{-1}$ in the final rounds of refinement were used. The most populated class was low-pass filtered to 60 Å and used as an initial reference for 3D classification of the full data set. For 2D and 3D classification in Relion, particles were re-extracted from the movie sums with the total dose of $35 \text{ e}^-/\text{\AA}^2$. 3D classification was carried out without application of symmetry operators. Only spatial frequencies up to $1/10 \text{ \AA}^{-1}$ were used to avoid overfitting. After 50 rounds of 3D classification with 4 classes, particles in 2 classes that produced similar 3D reconstructions were combined for 3D auto-refinement. The 3D reconstruction from ~27,000 particles was resolved to 14.1 Å (FSC = 0.143 criterion).

To obtain the final high-resolution 3D reconstructions, a data set of ~2,100 images was collected on a Titan Krios microscope (FEI) operated at 300 kV, equipped with a K2 Summit direct electron detector camera, operated in electron counting mode. Micrographs indicated monodisperse distribution of particles in ice (Supplementary Fig. 3a). Movie stacks were recorded at a nominal magnification of 22,500 \times , corresponding to a physical pixel size of 1.31 Å/pixel at a defocus range from $-1.0 \mu\text{m}$ to $-3.5 \mu\text{m}$. The rate of exposure was $2.91 \text{ e}^-/\text{\AA}^2/\text{s}$. 50-frame movie stacks were recorded for 17.5 s with an exposure of $1.02 \text{ e}^-/\text{\AA}^2$ per frame and a total electron dose of $51 \text{ e}^-/\text{\AA}^2$. Data collection was automated with SerialEM⁷³. Data collection statistics are in Table 2.

All image frames ($51 \text{ e}^-/\text{\AA}^2$ total dose) were aligned and summed with Unblur through the Relion pipeline^{68,70}. Defocus parameters were estimated from aligned sums of 5 frames using CTFFIND4 (ref. 69). Images were downsampled to a pixel size of 2.62 Å/pixel and ~403,023 manually picked particles were classified in 2D using Relion. Reference-free 2D class averages showed fine molecular features and presented the complex in different orientations, suggestive of its structural order and the lack of preferential orientation in ice (Supplementary Fig. 3b). After 3 rounds of the 2D classification ~197,779 particles were 3D classified into four classes without application of symmetry operators (Supplementary Fig. 4). The reconstruction from the TF20 data set was low-pass filtered to 60 Å and used as the initial reference for the 3D classification. 100 rounds of 3D classification with no applied symmetry produced two similar classes with a spiral conformation (~95,468 particles total, classes 2 and 4 in Supplementary Fig. 4), one class with a ring conformation (~48,565 particles, class 3 in Supplementary Fig. 4) with the rest of the particles classifying into a low-resolution class (~53,746 particles, class 1 in Supplementary Fig. 4). The low-resolution class consists of broken or misaligned particles and looked structurally different from the three major classes. Further classification of particles in this class did not identify any dominant conformation and did not improve the overall quality of the map. The particles from the two classes with the spiral conformation were combined and reclassified into 3 classes. All three classes looked alike and contained a similar number of particles, indicating the structural homogeneity of this particle set. Consequently, the particle set was refined in 3D as a single class. Similarly, the particle subset that produced the reconstruction with the ring conformation was further classified into two classes. Both new classes looked similar and contained a similar number of particles indicating the structural homogeneity of this particle set. Consequently, the original particle subset was refined in 3D as a single class.

For the 3D refinement, particles were re-extracted from unbinned image sums that showed tone rings to 5 Å or higher spatial frequencies. The 3D refinement was carried out using a created mask with a soft edge of six pixels to mask out flexible protein parts around the AAA ATPase hexameric core. Prior to application of the mask, no other well-defined features were visible outside the hexameric core. The 3D reconstruction of the spiral conformation was refined to 5.2 Å and the ring conformation to 7.3 Å (FSC = 0.143 criterion). To improve the quality of the 3D maps further, particles were sorted on the basis of their differences with their aligned, CTF-corrected references as described in refs. 46,74. A subset of particles with z scores ≤ 0.7 and ≤ 0.8 for the spiral and the ring conformations, respectively, were re-refined in 3D. This procedure improved the quality of the

final 3D maps with the resolution of the spiral reconstruction calculated to 4.4 Å and that of the planar reconstruction to 6.0 Å after implementation of the PostProcessing procedure with automatic masking and negative B -factor application. Both reconstructions were sharpened with the automatically determined negative B -factors of ~100 Å² for both structures. 38,072 and 16,185 particles contributed to the final maps in the spiral and ring conformations, respectively. Data collection statistics and image-processing summary are in Table 2.

To generate the difference maps in Figure 4 and Supplementary Figure 7, the atomic models for the protein were converted to mrc format using the bge routine in Bsoft⁷⁵ and low-pass filtered using the proc3d routine in EMAN⁷⁶. The difference maps for the spiral conformation between the cryo-EM reconstruction and the atomic model, low-pass filtered to either 5.5 Å for P1 and P6 or to 4.4 Å for P2 through P5, were generated using diffmap.exe (<http://grigoriefflab.janelia.org/software>). The resolution cutoff values for each protomer were determined by the blocres program in Bsoft⁷⁵. Atomic models for the ring conformation were low-pass filtered to 8 Å for P1 and P6 and to 6 Å for P2 through P5. The difference maps were generated following the procedure described for the spiral conformation.

Model building and refinement. Consistent with the estimation at 4.4-Å resolution, we observed grooves in α -helices, separated β -strands within β -sheets and densities for some bulky side chains. The X-ray structure of the katanin protomer was docked into the sharpened map using UCSF Chimera⁶¹, and its fit was improved with the collage option in Situs⁷⁷. The atomic model was fit flexibly into the cryo-EM reconstructions using NAMD with Molecular Dynamics Flexible Fitting (MDFF)⁷⁸. Secondary structure, chirality and *cis*-peptide restraints were applied to the model, and MDFF simulations were performed in implicit solvent at temperature $T = 300 \text{ K}$ to enhance the protein conformational sampling. Energy minimization was performed for 200 steps. MDFF simulations were carried out for 150 ps with a coupling constant (gscale) = 0.3. MDFF simulation convergence was monitored by plotting the r.m.s. deviation over time. Additional adjustments to the backbone and side chains for this model were performed manually in COOT⁵⁹, residue by residue. Densities for ATP were clearly visible in all six protomers of the spiral conformation (Fig. 4c–e and Supplementary Fig. 7a,c). The $\alpha 11$ – $\alpha 12$ linker, the C terminus and pore loop1 were built *de novo* as they are disordered in the monomer X-ray structure. Weak residual density features are present near pore loop1 that were not interpreted at the current resolution limit. None of the side chains of the pore-loop residues were built. The resulting model was subjected to real space refinement in PHENIX⁶⁰. The final atomic model has an overall correlation to the map of 0.791. For the ring conformation, the X-ray structure was first rigidly docked using Situs and then flexibly fitted using MDFF and COOT into the cryo-EM map as described for the spiral conformation. Additional adjustments to the backbone for this model were performed manually in COOT. Densities for ATP were clearly visible in five of the six AAA protomers (Fig. 4j and Supplementary Fig. 7b,d). The model was subjected to real space refinement in PHENIX. The final atomic model has an overall correlation to the map of 0.790. MolProbity was used to evaluate model geometry⁷⁹. Model statistics for both conformations are listed in Table 2.

ATPase and microtubule-severing assays. ATPase assays were performed at room temperature in BRB80 buffer, 50 mM KCl, 2.5 mM MgCl₂, 1 mM ATP, 10 μM taxol at a 50 nM katanin concentration. ATPase activities were measured using an EnzChek Phosphate Assay (Life Technologies). Initial rates were calculated from the linear portion of the reaction profiles after addition of 1 mM ATP. ATPase rates were adjusted by subtraction of the measured release of phosphate in the absence of ATP. Rates reported are means from four separate reactions.

Chambers for TIRF microscopy were assembled as previously described⁸⁰. GMPCPP brain microtubules containing 1% biotinylated tubulin and 20% HiLyte647-labeled tubulin were immobilized in the chamber with 2 mg/ml Neutravidin (Sigma) and imaged by TIRF or DIC microscopy in severing buffer (BRB80 buffer with 2 mg/ml casein, 14.3 mM 2-mercaptoethanol, 2.5% glycerol, 50 mM KCl, 2.5 mM MgCl₂, 1 mM ATP, 1% Pluronic F127 (Life Technologies) and oxygen scavengers prepared as described in ref. 80). The chamber was then perfused with 20 nM katanin in severing buffer. Severing rates were calculated by manual counting of severing events as a function of time as described previously³⁷.

A Life Sciences Reporting Summary for this paper is available.

- Data availability.** All data and constructs used in this study are available upon reasonable request from the corresponding author. Atomic coordinates and structure factors for the X-ray structure have been deposited in the wwPDB with accession code PDB 5WC1. EM maps and atomic coordinates for the cryo-EM models have been deposited in the EMDB and PDB with accession codes EMD-8794 and PDB 5WC0 (spiral conformation) and EMD-8796 and PDB 5WCB (ring conformation).
56. Schuck, P. Size-distribution analysis of macromolecules by sedimentation velocity ultracentrifugation and lamm equation modeling. *Biophys. J.* **78**, 1606–1619 (2000).
 57. Otwinowski, Z. & Minor, W. [20] Processing of X-ray diffraction data collected in oscillation mode. *Methods Enzymol.* **276**, 307–326 (1997).
 58. McCoy, A.J. *et al.* Phaser crystallographic software. *J. Appl. Crystallogr.* **40**, 658–674 (2007).
 59. Emsley, P. & Cowtan, K. Coot: model-building tools for molecular graphics. *Acta Crystallogr. D Biol. Crystallogr.* **60**, 2126–2132 (2004).
 60. Adams, P.D. *et al.* PHENIX: a comprehensive Python-based system for macromolecular structure solution. *Acta Crystallogr. D Biol. Crystallogr.* **66**, 213–221 (2010).
 61. Pettersen, E.F. *et al.* UCSF Chimera—a visualization system for exploratory research and analysis. *J. Comput. Chem.* **25**, 1605–1612 (2004).
 62. Glatter, V.O. & Kratsky, O. *Small Angle X-ray Scattering* (Academic Press, London, 1982).
 63. Mylonas, E. & Svergun, D.I. Accuracy of molecular mass determination of proteins in solution by small-angle X-ray scattering. *J. Appl. Crystallogr.* **40**, s245–s249 (2007).
 64. Svergun, D. Determination of the regularization parameter in indirect-transform methods using perceptual criteria. *J. Appl. Crystallogr.* **25**, 495–503 (1992).
 65. Rambo, R.P. & Tainer, J.A. Accurate assessment of mass, models and resolution by small-angle scattering. *Nature* **496**, 477–481 (2013).
 66. Svergun, D.I. Restoring low resolution structure of biological macromolecules from solution scattering using simulated annealing. *Biophys. J.* **76**, 2879–2886 (1999).
 67. Volkov, V.V. & Svergun, D.I. Uniqueness of ab initio shape determination in small-angle scattering. *J. Appl. Crystallogr.* **36**, 860–864 (2003).
 68. Grant, T. & Grigorieff, N. Measuring the optimal exposure for single particle cryo-EM using a 2.6 Å reconstruction of rotavirus VP6. *eLife* **4**, e06980 (2015).
 69. Rohou, A. & Grigorieff, N. CTFFIND4: Fast and accurate defocus estimation from electron micrographs. *J. Struct. Biol.* **192**, 216–221 (2015).
 70. Scheres, S.H. RELION: implementation of a Bayesian approach to cryo-EM structure determination. *J. Struct. Biol.* **180**, 519–530 (2012).
 71. Grigorieff, N. FREALIGN: high-resolution refinement of single particle structures. *J. Struct. Biol.* **157**, 117–125 (2007).
 72. Grigorieff, N. FREALIGN: an exploratory tool for single-particle cryo-EM. *Methods Enzymol.* **579**, 191–226 (2016).
 73. Mastronarde, D.N. Automated electron microscope tomography using robust prediction of specimen movements. *J. Struct. Biol.* **152**, 36–51 (2005).
 74. Chua, E.Y. *et al.* 3.9 Å structure of the nucleosome core particle determined by phase-plate cryo-EM. *Nucleic Acids Res.* **44**, 8013–8019 (2016).
 75. Heymann, J.B. Bsoft: image and molecular processing in electron microscopy. *J. Struct. Biol.* **133**, 156–169 (2001).
 76. Ludtke, S.J., Baldwin, P.R. & Chiu, W. EMAN: semiautomated software for high-resolution single-particle reconstructions. *J. Struct. Biol.* **128**, 82–97 (1999).
 77. Wriggers, W., Milligan, R.A. & McCammon, J.A. Situs: a package for docking crystal structures into low-resolution maps from electron microscopy. *J. Struct. Biol.* **125**, 185–195 (1999).
 78. Trabuco, L.G., Villa, E., Mitra, K., Frank, J. & Schulten, K. Flexible fitting of atomic structures into electron microscopy maps using molecular dynamics. *Structure* **16**, 673–683 (2008).
 79. Davis, I.W. *et al.* MolProbity: all-atom contacts and structure validation for proteins and nucleic acids. *Nucleic Acids Res.* **35**, W375–W383 (2007).
 80. Ziólkowska, N.E. & Roll-Mecak, A. In vitro microtubule severing assays. *Methods Mol. Biol.* **1046**, 323–334 (2013).

Life Sciences Reporting Summary

Nature Research wishes to improve the reproducibility of the work that we publish. This form is intended for publication with all accepted life science papers and provides structure for consistency and transparency in reporting. Every life science submission will use this form; some list items might not apply to an individual manuscript, but all fields must be completed for clarity.

For further information on the points included in this form, see [Reporting Life Sciences Research](#). For further information on Nature Research policies, including our [data availability policy](#), see [Authors & Referees](#) and the [Editorial Policy Checklist](#).

▶ Experimental design

1. Sample size

Describe how sample size was determined.

not applicable

Data exclusions

Describe any data exclusions.

none

Replication

Describe whether the experimental findings were reliably reproduced.

experiments were replicated in at least triplicate

Randomization

Describe how samples/organisms/participants were allocated into experimental groups.

not applicable

Blinding

Describe whether the investigators were blinded to group allocation during data collection and/or analysis.

not applicable

Note: all studies involving animals and/or human research participants must disclose whether blinding and randomization were used.

Statistical parameters

For all figures and tables that use statistical methods, confirm that the following items are present in relevant figure legends (or in the Methods section if additional space is needed).

Confirmed

- The exact sample size (n) for each experimental group/condition, given as a discrete number and unit of measurement (animals, litters, cultures, etc.)
 A description of how samples were collected, noting whether measurements were taken from distinct samples or whether the same sample was measured repeatedly
 A statement indicating how many times each experiment was replicated
 The statistical test(s) used and whether they are one- or two-sided (note: only common tests should be described solely by name; more complex techniques should be described in the Methods section)
 A description of any assumptions or corrections, such as an adjustment for multiple comparisons
 The test results (e.g. P values) given as exact values whenever possible and with confidence intervals noted
 A clear description of statistics including central tendency (e.g. median, mean) and variation (e.g. standard deviation, interquartile range)
 Clearly defined error bars

See the web collection on [statistics for biologists](#) for further resources and guidance.

► Software

Policy information about [availability of computer code](#)

7. Software

Describe the software used to analyze the data in this study.

HKL2000, Phenix, Coot, ctffind4, Frealign, Relion, Molprobit

For manuscripts utilizing custom algorithms or software that are central to the paper but not yet described in the published literature, software must be made available to editors and reviewers upon request. We strongly encourage code deposition in a community repository (e.g. GitHub). *Nature Methods* [guidance for providing algorithms and software for publication](#) provides further information on this topic.

► Materials and reagents

Policy information about [availability of materials](#)

8. Materials availability

Indicate whether there are restrictions on availability of unique materials or if these materials are only available for distribution by a for-profit company.

Coordinates and structure factors for the X-ray structure have been deposited in the PDB. Models and maps for the cryo-EM structures in the two conformations have been deposited in the PDB and EMDB.

Antibodies

Describe the antibodies used and how they were validated for use in the system under study (i.e. assay and species).

not applicable

Eukaryotic cell lines

a. State the source of each eukaryotic cell line used.

not applicable

b. Describe the method of cell line authentication used.

not applicable

c. Report whether the cell lines were tested for mycoplasma contamination.

not applicable

d. If any of the cell lines used are listed in the database of commonly misidentified cell lines maintained by [ICLAC](#), provide a scientific rationale for their use.

not applicable

Animals and human research participants

Policy information about [studies involving animals](#); when reporting animal research, follow the [ARRIVE guidelines](#)

1. Description of research animals

Provide details on animals and/or animal-derived materials used in the study.

not applicable

Policy information about [studies involving human research participants](#)

2. Description of human research participants

Describe the covariate-relevant population characteristics of the human research participants.

not applicable